Editors' Suggestion

Control of Néel Vector with Spin-Orbit Torques in an Antiferromagnetic Insulator with Tilted Easy Plane

Pengxiang Zhang,[1] Chung-Tao Chou,[1,2] Hwanhui Yun,[3] Brooke C. McGoldrick,[1]
Justin T. Hou,[1] K. Andre Mkhoyan,[3] and Luqiao Liu[1,*]
[1]*Department of Electrical Engineering and Computer Science, Massachusetts Institute of Technology, Cambridge, Massachusetts 02139, USA*
[2]*Department of Physics, Massachusetts Institute of Technology, Cambridge, Massachusetts 02139, USA*
[3]*Department of Chemical Engineering and Materials Science, University of Minnesota, Minneapolis, Minnesota 55455, USA*

(Received 5 February 2022; revised 29 April 2022; accepted 2 June 2022; published 1 July 2022)

Injecting spin currents into antiferromagnets and realizing efficient spin-orbit-torque switching represents a challenging topic. Because of the diminishing magnetic susceptibility, current-induced antiferromagnetic dynamics remain poorly characterized, complicated by spurious effects. Here, by growing a thin film antiferromagnet, α-Fe_2O_3, along its nonbasal plane orientation, we realize a configuration where the spin-orbit torque from an injected spin current can unambiguously rotate and switch the Néel vector within the tilted easy plane, with an efficiency comparable to that of classical ferrimagnetic insulators. Our study introduces a new platform for quantitatively characterizing switching and oscillation dynamics in antiferromagnets.

DOI: 10.1103/PhysRevLett.129.017203

Spin-orbit torque (SOT) switching of antiferromagnets has been extensively pursued recently with both antiferromagnet single layers owning staggered spin torques [1–6] and antiferromagnet–heavy metal bilayers [7–12]. In the latter case, it is expected that the spin Hall effect (SHE) from the neighboring heavy metal can act on the antiferromagnetic ordering and lead to Néel vector reorientation. Particularly, antiferromagnets with easy-plane anisotropy like NiO, CoO, and α-Fe_2O_3 have been utilized in these experiments for achieving multiple equilibrium positions of the Néel vector. Since the magnetic easy plane is usually also the crystalline plane with low surface energy, antiferromagnetic films are almost always synthesized with their surface coinciding with the magnetic easy plane, the geometry of which unfortunately poses extra difficulties for controlling magnetic ordering with SOT. As shown in Fig. 1(a), since spins generated from standard SHE [13,14] are oriented in plane at the antiferromagnet–heavy metal interface, the dampinglike torque τ_{DL}, if any, tends to rotate the Néel vector out of the film surface. In this configuration, τ_{DL} needs to overcome the very strong easy-plane anisotropy in order to realize precession or switching [15,16], resulting in formidable threshold currents. Spurious thermal effects such as electromigration and magnetoelastic effects also emerge due to the large applied current [11,17–21], further shadowing real SOT-related physics.

Efficient control over the Néel vector can be potentially achieved if the injected spins form a finite angle with the easy plane. As shown in Fig. 1(b), when the easy plane is no longer parallel with the film surface, the SOT from the injected in-plane spins will have a component facilitating the Néel vector rotation within the easy plane. In this configuration, the SOT only needs to overcome the much weaker anisotropy within the easy plane. Under a τ_{DL}, the effective fields on the normalized magnetic moments of the two sublattices $\boldsymbol{m}_{A(B)}$ have the form $\boldsymbol{H}_{\mathrm{DL}}^{A(B)} \propto \boldsymbol{m}_{A(B)} \times \boldsymbol{\sigma}$, which rotate the two sublattices constructively, in contrast to the effect of a magnetic field, which cancels between sublattices. Therefore, a threshold current similar to that in traditional ferromagnets can be anticipated. In this Letter, we realized the SOT configuration in Fig. 1(b) by growing antiferromagnetic thin film α-Fe_2O_3 with *R* plane, a nonbasal plane, orientation. Different from previously studied *C*-plane samples where the SOT effect remains hardly

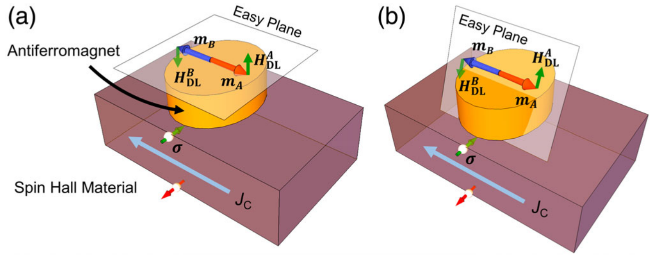

FIG. 1. (a) An antiferromagnet with its easy plane parallel with the film surface. Dampinglike torque effective fields $\boldsymbol{H}_{\mathrm{DL}}^{A(B)}$ rotate the two magnetic moments $\boldsymbol{m}_{A(B)}$ toward out-of-plane directions. (b) An antiferromagnet with the easy plane forming a finite angle with the film surface. $\boldsymbol{H}_{\mathrm{DL}}^{A(B)}$ have components for rotating $\boldsymbol{m}_{A(B)}$ within the easy plane.

detectable [18], SOT leads to efficient Néel vector rotation in this sample, which was further quantitatively calibrated with real magnetic fields. Utilizing SOT, we also achieved bipolar switching by applying positive and negative currents along the same path, in contrast to previously studied geometries utilizing two orthogonal currents [1,4,8]. Besides magnetic switching, the demonstrated configurations can also be utilized for low power antiferromagnetic oscillator [22], as well as magnon spin superfluidity [23–25] that have been predicted in previous literature.

α-Fe_2O_3 is an antiferromagnetic insulator with high Néel point (955 K) and easy-plane anisotropy at room temperature [26,27]. Because of the very weak magnetic anisotropy within the easy plane (C plane) [28], magnetic field needed for spin-flop transition is unusually low in this antiferromagnet (<1 Tesla), enabling people to control the Néel vector easily. Besides the common C-plane (0001) orientation, α-Fe_2O_3 thin film has also been grown along a few other low-index directions, including A-$(\bar{2}110)$ and R-plane $(01\bar{1}2)$ [Fig. 2(a)], both of which satisfy the finite angle requirement in Fig. 1(b). Meanwhile, to monitor the Néel vector through the spin Hall magnetoresistance (SMR), an oblique, rather than right angle between the easy plane and the sample surface is preferred [29]. Therefore, we choose to focus on R-plane films in this Letter, which are epitaxially grown on R-plane α-Al_2O_3 substrates [30]. As the R plane becomes the horizontal film surface, the easy plane (C plane) forms a tilting angle $\chi_{\text{tilt}} = 58°$ with the surface [Fig. 2(a)]. To reduce the strain from the lattice mismatch between α-Fe_2O_3 and α-Al_2O_3 (~5.8%), we deposit 1 nm of α-Cr_2O_3 prior to α-Fe_2O_3 as the seeding layer, which has an intermediate lattice constant. From magnetometry and electrical measurement as discussed below, we found that the 1 nm α-Cr_2O_3 behaves inactively, making negligible contribution to magnetic dynamics. The film structure is examined using x-ray diffraction (XRD) [Fig. 2(c)], where the $(01\bar{1}2)$ diffraction peak position agrees with the expected lattice constant and the film growth direction. The epitaxial growth is further verified through the XRD reciprocal space mapping [Fig. 2(d)], which, in combination with the scanning transmission electron microscope (STEM) image [Fig. 2(b)], shows that the strain is mostly relaxed at the film-substrate interface via misfit dislocations [30].

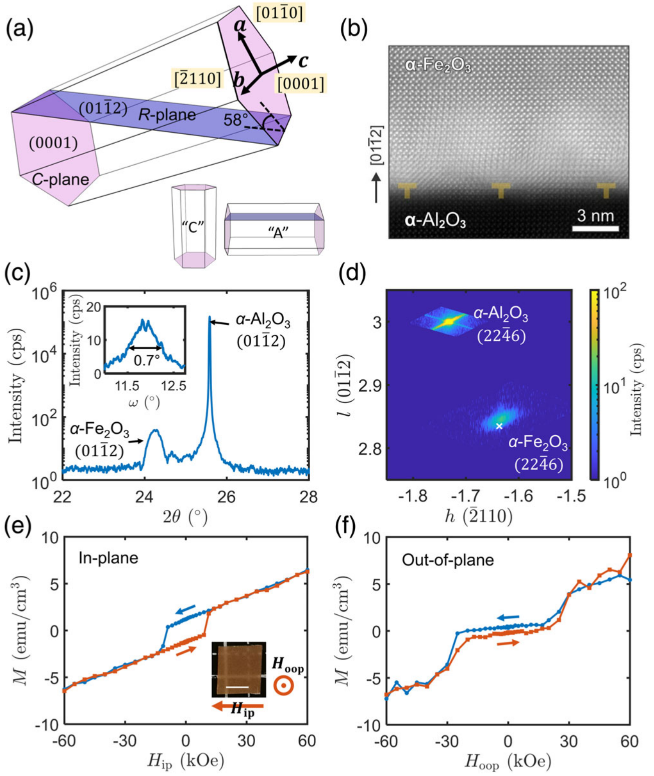

FIG. 2. (a) Unit cell of R-plane sample. Inset: unit cell orientation for C-plane ("C") and A-plane ("A") samples. (b) Cross-sectional atomic-resolution high-angle annular dark-field (HAADF) STEM image. Dislocation symbols are marked. (c) XRD symmetric 2θ-ω scan. "cps" represents counts per second. Inset: rocking curve. (d) Reciprocal space map. "x" represents the expected diffraction peak position if the strain in the film were fully relaxed. (e),(f) M-H loop for a 30 nm thick film under in-plane (e) and out-of-plane (f) field. Linear background at high fields comes from antiferromagnetic susceptibility. Inset of (e): Photo of the R-plane sample with the field direction labeled, which is ~45° counterclockwise from the $+b$ axis in the R plane of (a). The scale bar is 3 mm.

We characterize magnetic properties of the films using superconducting quantum interference device (SQUID) magnetometer at 300 K. When a field H is applied in the film plane along the cleavage edge of the sample, we see a typical M-H loop from canted antiferromagnetism [Fig. 2(e)]. It is known that in its easy-plane phase, sublattices in α-Fe_2O_3 form a small canting angle (<0.1°) through the Dzyaloshinskii-Moriya (DM) interaction [28], which induces a tiny net magnetization (1–$2\ \mathrm{emu/cm^3}$) and provides a handle for controlling the Néel vector. The measured small, finite magnetization therefore suggests that the R-plane sample remains in the easy-plane phase, similar to C-plane ones studied earlier. But different from C-plane samples with very low coercivity ($H_C \sim 1$ kOe), the R-plane sample has a larger H_C (10 kOe). Moreover, by applying field along the z axis, we also measure the out-of-film-plane M-H loop [Fig. 2(f)], where a spin-flop transition is observed, indicating additional, high order anisotropy develops on top of the standard easy-plane anisotropy. With M-H curves measured along different directions as well as electrical magnetoresistance measurements under rotating fields (discussed below), we conclude that a weak, uniaxial magnetic anisotropy exists within the C plane, with the easy axis along the $[0\bar{1}10]$ direction, or the a axis defined Fig. 2(a). This additional anisotropy is likely caused by the growth-induced symmetry breaking, where the residual strain distorts the hexagonal C plane along the a axis, making it the preferred axis through magnetoelastic effect. Here, we note that despite the increased in-plane H_C, it does not prevent us from observing SOT's effects since τ_{DL} acts constructively on the Néel vector [Fig. 1(b)] while the measured H_C reflects the field's effect which largely cancels between sublattices.

To study the SOT, we sputter 5 nm Pt on 30 nm R-plane α-Fe$_2$O$_3$ and fabricate Hall bars of 8 μm wide with the current channel aligned along $[\bar{2}110]$, [b axis in Fig. 3(a)]. We measure the transverse SMR at room temperature while applying a rotating field $\boldsymbol{H}$ within the xz plane, with the field angle β defined in Fig. 3(a). When the projected component of $\boldsymbol{H}$ on the C plane is larger than the spin-flop field, it will align the net moment $\boldsymbol{m}_{\mathrm{net}} = (\boldsymbol{m}_A + \boldsymbol{m}_B)/2$ parallel with, and the Néel vector $\boldsymbol{n} = (\boldsymbol{m}_A - \boldsymbol{m}_B)/2$ perpendicular to it. In Fig. 3(a), when a current flows along the x axis, spins $\boldsymbol{\sigma}$ polarized along y from the Pt SHE are injected into α-Fe$_2$O$_3$ and lead to antiferromagnetic SMR signal $R_H^{\mathrm{SMR}} = -R_0^{\mathrm{SMR}} n_x n_y = -\frac{1}{2} R_0^{\mathrm{SMR}} \sin 2\varphi \cos\chi_{\mathrm{tilt}}$, [29] where R_0^{SMR} is the transverse SMR amplitude, and $n_x = -\sin\varphi$ and $n_y = -\cos\varphi\cos\chi_{\mathrm{tilt}}$ are components of $\boldsymbol{n}$, with φ being the azimuthal angle [see Fig. 3(a)]. Figure 3(b) shows the measured R_H^{SMR} (or R_H^{ω} as in a first harmonic lock-in measurement) as a function of β under different field strengths, after an ordinary Hall resistance is subtracted. The ordinary Hall resistance from Pt linearly depends on the z component of $\boldsymbol{H}$ and can be calibrated in a standard way [30]. We see that R_H^{ω} has an angular dependence with 180° period, consistent with the $\sin(2\varphi)$ factor in its formula. Under lower magnetic fields ($H < 12$ kOe), R_H^{ω} exhibits magnetic hysteresis, while for $H > 20$ kOe, R_H^{ω} is smoother and agrees better with a sinusoidal function, consistent with the switching fields in Figs. 2(e) and 2(f). Moreover, in Fig. 3(b) we notice that the slopes for $-45° < \beta < 45°$ are flatter compared with the ones for $45° < \beta < 135°$, in agreement with the fact that the a axis is the easy axis within the easy plane. Besides the $\sin(2\beta)$ dependence, we find that R_H^{ω} in Fig. 3(b) has a small, residual component with a 360° periodicity, which maximizes (minimizes) for $\boldsymbol{H}$ along the $+z$ ($-z$) direction. This anomalous-Hall-like signal may originate from magnetic proximity or crystal Hall effect [30,35], both of which have the dependence of $R_H \propto m_z^{\mathrm{net}}$. Since this signal is small and can be separated from SMR via its angular dependence, we choose not to expand on its root origin.

The equilibrium orientation of $\boldsymbol{n}$, hence R_H^{SMR} under $\boldsymbol{H}$ can be determined via the magnetic free energy $F = E_Z + E_{\mathrm{ex}} + E_{\mathrm{DM}} + E_{\mathrm{an}}$. Here, the Zeeman, exchange, DM interaction and anisotropy energies are $E_Z = -\mu_0 M_0 (\boldsymbol{m}_A + \boldsymbol{m}_B) \cdot \boldsymbol{H}$, $E_{\mathrm{ex}} = \mu_0 M_0 H_{\mathrm{ex}} \boldsymbol{m}_A \cdot \boldsymbol{m}_B$, $E_{\mathrm{DM}} = -\mu_0 M_0 H_{\mathrm{DM}} \hat{\boldsymbol{c}} \cdot (\boldsymbol{m}_A \times \boldsymbol{m}_B)$, and $E_{\mathrm{an}} = K_1[(\boldsymbol{m}_A \cdot \hat{\boldsymbol{c}})^2 + (\boldsymbol{m}_B \cdot \hat{\boldsymbol{c}})^2] - K_2[(\boldsymbol{m}_A \cdot \hat{\boldsymbol{a}})^2 + (\boldsymbol{m}_B \cdot \hat{\boldsymbol{a}})^2]$, where μ_0 and M_0 are the vacuum permeability and the saturation magnetization of one sublattice, H_{ex} and H_{DM} are effective fields from exchange and DM interaction, K_1 and K_2 are energy densities for easy-plane and easy-axis anisotropy. Because of the very strong easy-plane anisotropy, $\boldsymbol{m}_A$ and $\boldsymbol{m}_B$ are mostly confined within the C plane in our experiment. As an approximation, we only consider their degrees of freedom within the C plane, quantified by the two angles φ and δ defined in Fig. 3(a). For a given $\boldsymbol{H}$, we can determine [30] the equilibrium angle φ_0, δ_0 through $[\partial F(\varphi, \delta)/\partial\varphi] = [\partial F(\varphi, \delta)/\partial\delta] = 0$. R_H^{SMR} is further calculated with its formula using φ_0, as shown by black lines in Fig. 3(b), which agree well with the experimental data. Using parameters reported in the literature [26,36,37]: $M_0 = 759$ emu/cm^3, $H_{\mathrm{ex}} = 9000$ kOe, $H_{\mathrm{DM}} = 17.8$ kOe, and $K_1 = 7.6 \times 10^4$ erg/cm^3, we determine the single fitting parameter $K_2 = 4.9 \times 10^3$ erg/cm^3, which universally fits all of the experimental curves.

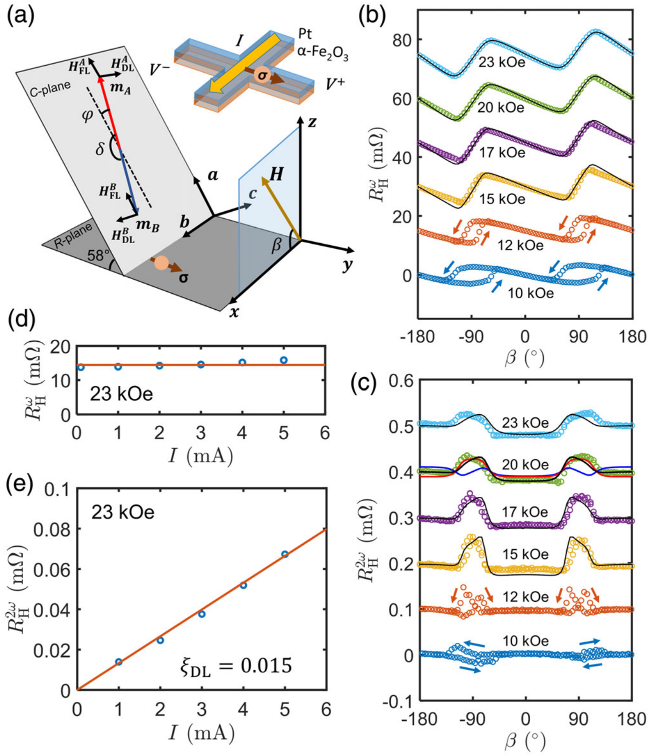

FIG. 3. (a) SOT geometry, with the current $\boldsymbol{I} \| \boldsymbol{x}$ and the injected spins $\boldsymbol{\sigma} \| \boldsymbol{y}$. $\boldsymbol{H}$ with an angle of β is applied within the xz plane. φ and δ define the angles of $\boldsymbol{n}$, and the spanning angle between $\boldsymbol{m}_{A(B)}$, respectively. Top-right inset: device illustration. (b),(c) First (b) and second (c) harmonic results of the transverse SMR as a function of β. The current is 4 mA (root mean square value). τ_{DL} (red) and τ_{FL} (blue) contributions to $R_H^{2\omega}$ at $H = 20$ kOe are separately plotted. (d),(e) Current dependence of R_H^{ω} and $R_H^{2\omega}$, taken at $H = 23$ kOe.

We quantify SOT by detecting the second harmonic resistance $R_H^{2\omega}$, as has been widely used in ferromagnets [38]. Theoretically $R_H^{2\omega}$ can be expressed as $R_H^{2\omega} = \frac{1}{2}(dR_H^{\omega}/d\varphi)|_{\varphi_0} \cdot \Delta\varphi(I)$, where $(dR_H^{\omega}/d\varphi)|_{\varphi_0}$ is calculated from SMR's formula, and $\Delta\varphi(I)$ is the SOT induced $\boldsymbol{n}$ rotation from its equilibrium φ_0, $\Delta\varphi(I)$ can be determined through the balance between SOT and the torque due to the magnetic free energy $\tau_{\mathrm{ST}}(I) + \tau_{\mathrm{M}}(I) = 0$, with $\tau_{\mathrm{ST}}(I)$ consisting of $\tau_{\mathrm{DL(FL)}} = -\mu_0 M_0 (\boldsymbol{m}_A \times \mu_0 \boldsymbol{H}^A_{\mathrm{DL(FL)}} + \boldsymbol{m}_B \times \mu_0 \boldsymbol{H}^B_{\mathrm{DL(FL)}}) \cdot \hat{\boldsymbol{c}}$ and $\tau_M(I)$ being $\tau^{\varphi}_M(I) \approx -(\partial F/\partial \varphi)|_{\varphi_0 + \Delta\varphi(I)}$. Here, $\boldsymbol{H}_{\mathrm{DL}}$ ($\boldsymbol{H}_{\mathrm{FL}}$) are the dampinglike (fieldlike) effective fields on individual sublattices, and H_{DL} is further related to the spin Hall efficiency ξ through $H_{\mathrm{DL}} = \frac{1}{2}(\hbar \xi J_C / 2e\mu_0 M_0 t)$ [34,39], where $\hbar$, e, μ_0, J_C, and t are the reduced Planck constant, electron charge, permeability of vacuum, current density in Pt, and α-$\mathrm{Fe_2O_3}$ thickness. For the measured $R_H^{2\omega}$ in Fig. 3(c), outside the hysteresis region ($H \geq 15$ kOe), $R_H^{2\omega}$ has peaks close to $\beta = \pm 90°$, and the peak magnitude decreases when H increases. The position and the field magnitude dependence of $R_H^{2\omega}$ are consistent with signatures of SOT. First, at $\beta = \pm 90°$, the slope of $(dR_H^{\omega}/d\beta)$ (and similarly $(dR_H^{\omega}/d\varphi)$) reaches maximum in Fig. 3(b), which therefore converts $\boldsymbol{n}$ rotation to $R_H^{2\omega}$ most efficiently. Second, a higher H pins $\boldsymbol{n}$ more strongly, and suppresses the rotation, resulting in a smaller $R_H^{2\omega}$. We also verify that $R_H^{2\omega}$ is proportional to the current [Fig. 3(e)], as expected from the SOT mechanism, while R_H^{ω} shows no current dependence [Fig. 3(d)]. $R_H^{2\omega}$ can be calculated [30] as

$$R_H^{2\omega} \approx R_0^{\mathrm{SMR}} \cos\chi_{\mathrm{tilt}} \cos 2\varphi_0 \frac{H_{\mathrm{DL}} \sin\chi_{\mathrm{tilt}} + H_{\mathrm{FL}} \cos\chi_{\mathrm{tilt}} \cos\frac{\delta_0}{2} \cos\varphi_0}{(4K_2 \cos 2\varphi_0 \cos\delta_0)/\mu_0 M_0 - 2H \cos\frac{\delta_0}{2} (\cos\beta \cos\varphi_0 + \sin\chi_{\mathrm{tilt}} \sin\beta \sin\varphi_0)}. \tag{1}$$

Here, we neglect the very small contribution from Oersted field, which has similar symmetry with H_{FL}. Equation (1) shows that τ_{DL} and τ_{FL} own different angle dependences [see red and blue lines for $H = 20$ kOe in Fig. 3(c)], allowing independent determination of the two. We fit the data in Fig. 3(c) with ξ and H_{FL} as the only fitting parameters, as shown by the black lines. From the fitting, we obtain $\xi = 0.015$ and $H_{\mathrm{FL}} = 100$ Oe under a current of $1.4 \times 10^7\ \mathrm{A/cm^2}$, translating into $\tau_{\mathrm{DL}} = 200\ \mathrm{erg/cm^3}$ (independent of φ_0) and $\tau_{\mathrm{FL}} = 150\ \mathrm{erg/cm^3}$ (maximum value at $\varphi_0 = 0°$). ξ is smaller than the intrinsic spin Hall angle of Pt ($0.05 \sim 0.3$) [39,40], but comparable to values reported in the Pt-ferrimagnetic insulator [41,42], probably due to a lower spin-mixing conductance with insulating material. The similar magnitude in dampinglike SOT between ferromagnet and antiferromagnet therefore proves that τ_{DL} can be an efficient mechanism for controlling $\boldsymbol{n}$ in this geometry.

The SOT origin of the measured signal is further verified through control experiments by flipping the current and voltage terminals, i.e., applying current along y and measuring voltage along x in Fig. 3(a). Now the injected spins lie within the C plane and τ_{DL} causes an out-of-easy-plane rotation, similar to Fig. 1(a). The negligible signal from dampinglike torque in our observation therefore agrees with this [30]. Meanwhile, our measurement is also insensitive to thermal effects including the magnetoelastic effect because for any thermal cause, the $\boldsymbol{n}$ tilting will depend linearly on the temperature variation, and quadratically on I, which gives rise to $R_H^{3\omega}$ rather than $R_H^{2\omega}$.

Besides the harmonic measurement with ac, the rotation of $\boldsymbol{n}$ can also be more intuitively captured through a direct current (dc) measurement. In Fig. 1(b), the role of τ_{DL} is to cause an almost constant rotation on $\boldsymbol{n}$ when β is varied, which will result in a horizontal shift in the $R_H^{\mathrm{SMR}} - \beta$ curve. This is demonstrated in Fig. 4(a) for $I = \pm 6$ mA, with a systematic shift of $\Delta\beta$ between the two curves, whose direction agrees with the sign of τ_{DL} determined from the harmonic measurement. Since we compare $\pm I$ with the same magnitude, artifacts with thermal origins get canceled. We note that the waveforms of dc SMR in Fig. 4(a) are not exactly the same with the ac results in Fig. 3(b), and the latter has stronger hysteresis. This is because we conditioned the samples with a large current (11 mA) before dc measurements, as previous studies show the current-induced annealing can change magnetic anisotropy and make the dc measurement more repeatable [11]. When H is much larger than the anisotropy field, we can assume the current induced $\boldsymbol{n}$ rotation roughly follows the angle shift of $\boldsymbol{H}$, i.e., $\Delta\varphi \approx \Delta\beta$. In Fig. 4(b) we summarize $\Delta\beta$ measured under different currents and fields, where $\Delta\beta$ scales proportionally with I and inversely proportionally with H, agreeing with the expected value [30] $\Delta\varphi \approx [H_{\mathrm{DL}} \sin\chi_{\mathrm{tilt}}/H \cos(\delta_0/2)]$. Linear fittings in Fig. 4(b) lead to $\xi_{\mathrm{DL}} = 0.018 \pm 0.003$, close to the $R_H^{2\omega}$ results.

Using the titled easy plane geometry, we also observe a current-induced switching. Figure 4(e) shows R_H^{SMR} measured with a small dc sensing current (1 mA) after applying positive or negative single current pulse (15 ms) along the same channel, where finite differences in the remnant R_H^{SMR} values develop for $|I| \geq 13$ mA. During this measurement, a constant H close to the spin-flop field is applied along the z axis, to compensate the in-plane anisotropy field and assist the switching [23]. Switchings only happen under intermediate fields (4 kOe $\leq |H_z| \leq$ 6 kOe) [Fig. 4(f)] as the net effective field is low after the compensation [30]. Nonmagnetic or thermal artifacts can be excluded as they are insensitive to fields, or current sign. The partial and nonvolatile switching can be understood through Fig. 4(c): τ_{DL} under a positive (negative) current rotates $\boldsymbol{n}$ clockwise (counterclockwise) and causes a $\Delta R_H^{\mathrm{SMR}}$. In Fig. 4(f), the

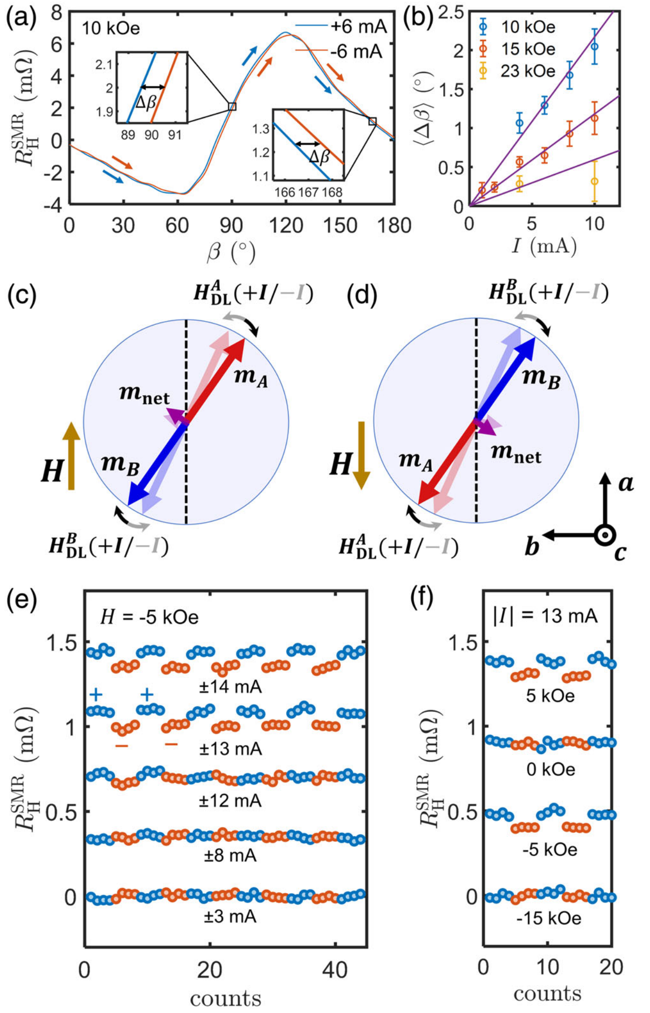

FIG. 4. (a) R_H^{SMR} under dc of $I = \pm 6$ mA. The insets show a magnified view of two curves to illustrate the horizontal shift angle $\Delta\beta$. (b) Summary on $\Delta\beta(I)$ under different $\boldsymbol{H}$, taking an average across all β values. (c),(d) Current-induced $\boldsymbol{n}$ rotation in the C plane for positive (c) and negative (d) field. The darker (lighter) arrows represent the position of $\boldsymbol{n}$ after positive (negative) current pulses. (e) Switching of R_H^{SMR} under current pulses with different magnitudes. The blue (red) dots show R_H^{SMR} after positive (negative) pulses. (f) Current-induced switching of R_H^{SMR} with different H. Switching is observed for intermediate fields and the polarity remains the same between $H_z = \pm 5$ kOe.

polarity of $\Delta R_H^{\mathrm{SMR}}$ remains the same for $H = \pm 5$ kOe. This is explained by comparing Figs. 4(c) and 4(d), where the rotation direction of $\boldsymbol{n}$ under a pair of $\pm I$ remains the same $2\Delta\varphi(I)$, independent on the H sign. Meanwhile, the H reversal changes the equilibrium angle of $\boldsymbol{n}$ from φ_0 to $\varphi_0 + 180°$, which does not affect the SMR with 180° periodicity. $\Delta R_H^{\mathrm{SMR}} = -R_0^{\mathrm{SMR}} \cos\chi_{\mathrm{tilt}} \cos 2\varphi_0 \cdot 2\Delta\varphi(I)$ is therefore the same between the positive and negative H cases. Finally, we note that the bipolar switching in our experiment represents a different switching mode compared to previous demonstrations with antiferromagnets where current pulses are usually applied along two orthogonal channels. The single current channel geometry employed here allows more compact design for practical applications. Our switching magnitude is still relatively small, corresponding to ∼2% of the total SMR. This small portion can be related to the weak hysteresis in the magnetization loop [Fig. 2(f)], where two remnant states under the same H_z bear small differences. Future efforts on increasing the remanence may enhance the switching.

To conclude, we experimentally demonstrate and quantify current-induced magnetic rotation in an antiferromagnetic insulator with a tilted easy plane. Spins injected along an oblique angle with respect to the easy plane provide an efficient mechanism to reorient Néel vectors. Aside from this titled geometry, the finite angle can also be achieved by using SHE materials with reduced symmetry like $\mathrm{WTe_2}$, $\mathrm{Mn_3GaN}$, and $\mathrm{Mn_3Ir}$, where an out-of-film-surface spin component can be generated from the nonconventional SHE [43–46]. The concept proved in our experiment can also help to investigate a rich family of antiferromagnetic dynamics such as terahertz spin torque oscillation and spin superfluidity.

This work is supported by National Science Foundation under Award No. DMR-2104912, AFOSR through Award No. FA9550-19-1-0048, and Semiconductor Research Corporation SMART center. P. Z. acknowledges support from Mathworks fellowship. H. Y. and K. A. M. were partially supported by University of Minnesota (UMN) MRSEC program DMR-2011401. The electron microscopy work was carried out in the Characterization Facility of University of Minnesota supported in part by the NSF through the UMN MRSEC.

---

[*] luqiao@mit.edu

[1] P. Wadley *et al.*, Electrical switching of an antiferromagnet, Science **351**, 587 (2016).

[2] M. J. Grzybowski, P. Wadley, K. W. Edmonds, R. Beardsley, V. Hills, R. P. Campion, B. L. Gallagher, J. S. Chauhan, V. Novak, T. Jungwirth, F. Maccherozzi, and S. S. Dhesi, Imaging Current-Induced Switching of Antiferromagnetic Domains in CuMnAs, Phys. Rev. Lett. **118**, 057701 (2017).

[3] J. Godinho, H. Reichlová, D. Kriegner, V. Novák, K. Olejník, Z. Kašpar, Z. Šobáň, P. Wadley, R. P. Campion, R. M. Otxoa, P. E. Roy, J. Železný, T. Jungwirth, and J. Wunderlich, Electrically induced and detected Néel vector reversal in a collinear antiferromagnet, Nat. Commun. **9**, 4686 (2018).

[4] S. Y. Bodnar, L. Šmejkal, I. Turek, T. Jungwirth, O. Gomonay, J. Sinova, A. A. Sapozhnik, H. J. Elmers, M. Kläui, and M. Jourdan, Writing and reading antiferromagnetic $\mathrm{Mn_2Au}$ by Néel spin-orbit torques and large anisotropic magnetoresistance, Nat. Commun. **9**, 348 (2018).

[5] M. Meinert, D. Graulich, and T. Matalla-Wagner, Electrical Switching of Antiferromagnetic $\mathrm{Mn_2Au}$ and the Role of Thermal Activation, Phys. Rev. Applied **9**, 064040 (2018).

[6] X. F. Zhou, J. Zhang, F. Li, X. Z. Chen, G. Y. Shi, Y. Z. Tan, Y. D. Gu, M. S. Saleem, H. Q. Wu, F. Pan, and C. Song, Strong Orientation-Dependent Spin-Orbit Torque in Thin Films of the Antiferromagnet Mn_2Au, Phys. Rev. Applied **9**, 054028 (2018).

[7] T. Moriyama, K. Oda, T. Ohkochi, M. Kimata, and T. Ono, Spin torque control of antiferromagnetic moments in NiO, Sci. Rep. **8**, 14167 (2018).

[8] X. Z. Chen, R. Zarzuela, J. Zhang, C. Song, X. F. Zhou, G. Y. Shi, F. Li, H. A. Zhou, W. J. Jiang, F. Pan, and Y. Tserkovnyak, Antidamping-Torque-Induced Switching in Biaxial Antiferromagnetic Insulators, Phys. Rev. Lett. **120**, 207204 (2018).

[9] L. Baldrati, C. Schmitt, O. Gomonay, R. Lebrun, R. Ramos, E. Saitoh, J. Sinova, and M. Kläui, Efficient Spin Torques in Antiferromagnetic CoO/Pt Quantified by Comparing Field- and Current-Induced Switching, Phys. Rev. Lett. **125**, 077201 (2020).

[10] I. Gray, T. Moriyama, N. Sivadas, G. M. Stiehl, J. T. Heron, R. Need, B. J. Kirby, D. H. Low, K. C. Nowack, D. G. Schlom, D. C. Ralph, T. Ono, and G. D. Fuchs, Spin Seebeck Imaging of Spin-Torque Switching in Antiferromagnetic Pt/NiO Heterostructures, Phys. Rev. X **9**, 041016 (2019).

[11] Y. Cheng, S. Yu, M. Zhu, J. Hwang, and F. Yang, Electrical Switching of Tristate Antiferromagnetic Néel Order in α-Fe_2O_3 Epitaxial Films, Phys. Rev. Lett. **124**, 027202 (2020).

[12] Y. Takeuchi, Y. Yamane, J.-Y. Yoon, R. Itoh, B. Jinnai, S. Kanai, J. i. Ieda, S. Fukami, and H. Ohno, Chiral-spin rotation of non-collinear antiferromagnet by spin-orbit torque, Nat. Mater. **20**, 1364 (2021).

[13] J. E. Hirsch, Spin Hall Effect, Phys. Rev. Lett. **83**, 1834 (1999).

[14] S. F. Zhang, Spin Hall Effect in the Presence of Spin Diffusion, Phys. Rev. Lett. **85**, 393 (2000).

[15] H. V. Gomonay and V. M. Loktev, Spin transfer and current-induced switching in antiferromagnets, Phys. Rev. B **81**, 144427 (2010).

[16] R. Zarzuela and Y. Tserkovnyak, Antiferromagnetic textures and dynamics on the surface of a heavy metal, Phys. Rev. B **95**, 180402(R) (2017).

[17] C. C. Chiang, S. Y. Huang, D. Qu, P. H. Wu, and C. L. Chien, Absence of Evidence of Electrical Switching of the Antiferromagnetic Néel Vector, Phys. Rev. Lett. **123**, 227203 (2019).

[18] P. Zhang, J. Finley, T. Safi, and L. Liu, Quantitative Study on Current-Induced Effect in an Antiferromagnet Insulator/Pt Bilayer Film, Phys. Rev. Lett. **123**, 247206 (2019).

[19] A. Churikova, D. Bono, B. Neltner, A. Wittmann, L. Scipioni, A. Shepard, T. Newhouse-Illige, J. Greer, and G. S. D. Beach, Non-magnetic origin of spin Hall magnetoresistance-like signals in Pt films and epitaxial NiO/Pt bilayers, Appl. Phys. Lett. **116**, 022410 (2020).

[20] L. Baldrati, O. Gomonay, A. Ross, M. Filianina, R. Lebrun, R. Ramos, C. Leveille, F. Fuhrmann, T. R. Forrest, F. Maccherozzi, S. Valencia, F. Kronast, E. Saitoh, J. Sinova, and M. Kläui, Mechanism of Néel Order Switching in Antiferromagnetic Thin Films Revealed by Magnetotransport and Direct Imaging, Phys. Rev. Lett. **123**, 177201 (2019).

[21] H. Meer, F. Schreiber, C. Schmitt, R. Ramos, E. Saitoh, O. Gomonay, J. Sinova, L. Baldrati, and M. Kläui, Direct imaging of current-induced antiferromagnetic switching revealing a pure thermomagnetoelastic switching mechanism in NiO, Nano Lett. **21**, 114 (2021).

[22] O. R. Sulymenko, O. V. Prokopenko, V. S. Tiberkevich, A. N. Slavin, B. A. Ivanov, and R. S. Khymyn, Terahertz-Frequency Spin Hall Auto-oscillator Based on a Canted Antiferromagnet, Phys. Rev. Applied **8**, 064007 (2017).

[23] A. Qaiumzadeh, H. Skarsvåg, C. Holmqvist, and A. Brataas, Spin Superfluidity in Biaxial Antiferromagnetic Insulators, Phys. Rev. Lett. **118**, 137201 (2017).

[24] H. Chen and A. H. MacDonald, in *Universal Themes of Bose-Einstein Condensation*, edited by David W. Snoke, Nick P. Proukakis, and Peter B. Littlewood (Cambridge University Press, Cambridge, England, 2017), pp. 525-548.

[25] S. Takei, B. I. Halperin, A. Yacoby, and Y. Tserkovnyak, Superfluid spin transport through antiferromagnetic insulators, Phys. Rev. B **90**, 094408 (2014).

[26] S. J. Williamson and S. Foner, Antiferromagnetic resonance in systems with Dzyaloshinsky-Moriya coupling; orientation dependence in αFe_2O_3, Phys. Rev. **136**, A1102 (1964).

[27] R. Lebrun, A. Ross, S. A. Bender, A. Qaiumzadeh, L. Baldrati, J. Cramer, A. Brataas, R. A. Duine, and M. Kläui, Tunable long-distance spin transport in a crystalline antiferromagnetic iron oxide, Nature (London) **561**, 222 (2018).

[28] P. J. Flanders and J. P. Remeika, Magnetic properties of hematite single crystals, Philos. Mag. A **11**, 1271 (1965).

[29] L. Baldrati, A. Ross, T. Niizeki, C. Schneider, R. Ramos, J. Cramer, O. Gomonay, M. Filianina, T. Savchenko, D. Heinze, A. Kleibert, E. Saitoh, J. Sinova, and M. Kläui, Full angular dependence of the spin Hall and ordinary magnetoresistance in epitaxial antiferromagnetic NiO(001)/Pt thin films, Phys. Rev. B **98**, 024422 (2018).

[30] See Supplemental Material at http://link.aps.org/supplemental/10.1103/PhysRevLett.129.017203, which includes Refs. [31–34], for details on materials growth and characterization, spin Hall magnetoresistance measurements and modeling, and discussions about current-induced nonvolatile switching.

[31] N. Shimomura, S. P. Pati, Y. Sato, T. Nozaki, T. Shibata, K. Mibu, and M. Sahashi, Morin transition temperature in (0001)-oriented α-Fe_2O_3 thin film and effect of Ir doping, J. Appl. Phys. **117**, 17C736 (2015).

[32] T. Fujii, M. Takano, R. Kakano, Y. Isozumi, and Y. Bando, Spin-flip anomalies in epitaxial α-Fe_2O_3 films by Mössbauer spectroscopy, J. Magn. Magn. Mater. **135**, 231 (1994).

[33] S. Gota, M. Gautier-Soyer, and M. Sacchi, Magnetic properties of $Fe_2O_3(0001)$ thin layers studied by soft x-ray linear dichroism, Phys. Rev. B **64**, 224407 (2001).

[34] J. Han, P. Zhang, Z. Bi, Y. Fan, T. S. Safi, J. Xiang, J. Finley, L. Fu, R. Cheng, and L. Liu, Birefringence-like spin transport via linearly polarized antiferromagnetic magnons, Nat. Nanotechnol. **15**, 563 (2020).

[35] L. Šmejkal, R. González-Hernández, T. Jungwirth, and J. Sinova, Crystal time-reversal symmetry breaking and spontaneous Hall effect in collinear antiferromagnets, Sci. Adv. **6**, eaaz8809 (2020).

[36] P. R. Elliston and G. J. Troup, Some antiferromagnetic resonance measurements in α-Fe_2O_3, J. Phys. C **1**, 169 (1968).

[37] K. Mizushima and S. Iida, Effective in-plane anisotropy field in αFe_2O_3, J. Phys. Soc. Jpn. **21**, 1521 (1966).

[38] J. Kim, J. Sinha, M. Hayashi, M. Yamanouchi, S. Fukami, T. Suzuki, S. Mitani, and H. Ohno, Layer thickness dependence of the current-induced effective field vector in Ta|CoFeB|MgO, Nat. Mater. **12**, 240 (2013).

[39] L. Liu, O. Lee, T. Gudmundsen, D. Ralph, and R. Buhrman, Current-Induced Switching of Perpendicularly Magnetized Magnetic Layers using Spin Torque from the Spin Hall Effect, Phys. Rev. Lett. **109**, 096602 (2012).

[40] M.-H. Nguyen, D. C. Ralph, and R. A. Buhrman, Spin Torque Study of the Spin Hall Conductivity and Spin Diffusion Length in Platinum Thin Films with Varying Resistivity, Phys. Rev. Lett. **116**, 126601 (2016).

[41] C. Hahn, G. de Loubens, O. Klein, M. Viret, V. V. Naletov, and J. Ben Youssef, Comparative measurements of inverse spin Hall effects and magnetoresistance in YIG/Pt and YIG/Ta, Phys. Rev. B **87**, 174417 (2013).

[42] C. O. Avci, A. Quindeau, C.-F. Pai, M. Mann, L. Caretta, A. S. Tang, M. C. Onbasli, C. A. Ross, and G. S. D. Beach, Current-induced switching in a magnetic insulator, Nat. Mater. **16**, 309 (2017).

[43] D. MacNeill, G. M. Stiehl, M. H. D. Guimaraes, R. A. Buhrman, J. Park, and D. C. Ralph, Control of spin-orbit torques through crystal symmetry in WTe_2/ferromagnet bilayers, Nat. Phys. **13**, 300 (2017).

[44] T. Nan *et al.*, Controlling spin current polarization through noncollinear antiferromagnetism, Nat. Commun. **11**, 4671 (2020).

[45] Y. Liu, Y. Liu, M. Chen, S. Srivastava, P. He, K. L. Teo, T. Phung, S.-H. Yang, and H. Yang, Current-Induced Out-of-Plane Spin Accumulation on the (001) Surface of the $IrMn_3$ Antiferromagnet, Phys. Rev. Applied **12**, 064046 (2019).

[46] Y. Zhang, Y. Sun, H. Yang, J. Železný, S. P. P. Parkin, C. Felser, and B. Yan, Strong anisotropic anomalous Hall effect and spin Hall effect in the chiral antiferromagnetic compounds Mn_3X ($X = $ Ge, Sn, Ga, Ir, Rh, and Pt), Phys. Rev. B **95**, 075128 (2017).